

Cavity-enhanced second-harmonic generation via nonlinear-overlap optimization

ZIN LIN,¹ XIANGDONG LIANG,² MARKO LONČAR,¹ STEVEN G. JOHNSON,² AND ALEJANDRO W. RODRIGUEZ^{3,*}

¹John A. Paulson School of Engineering and Applied Sciences, Harvard University, Cambridge, Massachusetts 02138, USA

²Department of Mathematics, Massachusetts Institute of Technology, Cambridge, Massachusetts 02139, USA

³Department of Electrical Engineering, Princeton University, Princeton, New Jersey 08544, USA

*Corresponding author: arod@princeton.edu

Received 13 November 2015; revised 26 January 2016; accepted 27 January 2016 (Doc. ID 253839); published 1 March 2016

We describe a novel approach based on topology optimization that enables automatic discovery of wavelength-scale photonic structures for achieving high-efficiency second-harmonic generation (SHG). A key distinction from previous formulation and designs that seek to maximize Purcell factors at individual frequencies is that our method aims to not only achieve frequency matching (across an entire octave) and large radiative lifetimes, but also optimizes the equally important nonlinear-coupling figure of merit $\bar{\beta}$, involving a complicated spatial overlap-integral between modes. We apply this method to the particular problem of optimizing micropost and grating-slab cavities (one-dimensional multilayered structures) and demonstrate that a variety of material platforms can support modes with the requisite frequencies, large lifetimes $Q > 10^4$, small modal volumes $\sim (\lambda/n)^3$, and extremely large $\bar{\beta} \gtrsim 10^{-2}$, leading to orders of magnitude enhancements in SHG efficiency compared to state-of-the-art photonic designs. Such giant $\bar{\beta}$ alleviate the need for ultranarrow linewidths and thus pave the way for wavelength-scale SHG devices with faster operating timescales and higher tolerance to fabrication imperfections. © 2016 Optical Society of America

OCIS codes: (190.0190) Nonlinear optics; (050.1755) Computational electromagnetic methods.

<http://dx.doi.org/10.1364/OPTICA.3.000233>

1. INTRODUCTION

Nonlinear optical processes mediated by second-order ($\chi^{(2)}$) nonlinearities play a crucial role in many photonic applications, including ultrashort-pulse shaping [1,2], spectroscopy [3], generating novel states of light [4–6], and quantum information processing [7–9]. Because nonlinearities are generally weak in bulk media, a well-known approach for lowering the power requirements of devices is to enhance nonlinear interactions by employing optical resonators that confine light for long times (larger quality factors Q) in small volumes V [10–19]. Microcavity resonators designed for on-chip, infrared applications offer some of the smallest confinement factors available, but their implementation in practical devices has been largely hampered by the difficult task of identifying wavelength-scale ($V \sim \lambda^3$) structures supporting long-lived, resonant modes at widely separated wavelengths and satisfying rigid frequency-matching and mode-overlap constraints [15,20].

In this article, we extend a recently proposed formulation for the scalable topology optimization of microcavities, where every pixel of the geometry is a degree of freedom, to the problem of designing wavelength-scale photonic structures for second-harmonic generation (SHG). We apply this approach to obtain novel micropost and grating microcavity designs supporting strongly coupled fundamental and harmonic modes at infrared and visible wavelengths with relatively large lifetimes $Q_1, Q_2 > 10^4$. In contrast to recently proposed designs based on known, linear cavity structures hand

tailored to maximize the Purcell factors or minimize mode volumes of individual resonances, e.g., ring resonators [17,21–23] and nanobeam cavities [19,24], our designs ensure frequency matching and small confinement factors, while simultaneously maximizing the SHG enhancement factor $Q_1^2 Q_2 |\bar{\beta}|^2$ to yield orders of magnitude improvements in the nonlinear coupling $\bar{\beta}$ described by Eq. (3) and determined by a special overlap integral between the modes. These particular optimizations of multilayer stacks illustrate the benefits of our formalism in an approachable and experimentally feasible setting, laying the framework for future topology optimization of 2D/3D slab structures that are sure to yield even further improvements. In what follows, although we will primarily focus on the problem of SHG as a concrete demonstration of our technique, the proposed formulation can be extended to many other problems of interest. For instance, in the area of quantum science and technology, where quantum information carried by photons needs to be communicated over long distance, our technique can be used to realize efficient quantum frequency conversion over the widest range, including that from visible to telecommunication wavelengths [25]. In fact, any nonlinear frequency conversion problem that can stand to benefit from a chip-scale nanophotonic platform can potentially benefit from this approach. Our work constitutes a new approach to nonlinear photonic design based on specially tailored aperiodic structures rather than conventional hand designs.

Most experimental demonstrations of SHG in chip-based photonic systems [16,17,23,26–29] operate in the so-called small-signal regime, where the lack of pump depletion leads to the well-known quadratic scaling of harmonic output with incident power [30]. In situations involving all-resonant conversion, where confinement and long interaction times lead to strong nonlinearities and non-negligible downconversion [12,20], the maximum achievable conversion efficiency ($\eta \equiv \frac{P_2^{\text{out}}}{P_1^{\text{in}}}$),

$$\eta^{\text{max}} = \left(1 - \frac{Q_1}{Q_1^{\text{rad}}}\right) \left(1 - \frac{Q_2}{Q_2^{\text{rad}}}\right), \quad (1)$$

occurs at a critical input power [20],

$$P_1^{\text{crit}} = \frac{2\omega_1 \epsilon_0 \lambda_1^3}{(\chi_{\text{eff}}^{(2)})^2 |\tilde{\beta}|^2 Q_1^2 Q_2} \left(1 - \frac{Q_1}{Q_1^{\text{rad}}}\right)^{-1}, \quad (2)$$

where $\chi_{\text{eff}}^{(2)}$ is the effective nonlinear susceptibility of the medium (Supplement 1), and $Q = (\frac{1}{Q^{\text{rad}}} + \frac{1}{Q^c})^{-1}$ is the dimensionless quality factor (ignoring material absorption) incorporating radiative decay $\frac{1}{Q^{\text{rad}}}$ and coupling to an input/output channel $\frac{1}{Q^c}$. The dimensionless coupling coefficient $\tilde{\beta}$ is given by a complicated, spatial-overlap integral involving the fundamental and harmonic modes (see Supplement 1 for details):

$$\tilde{\beta} = \frac{\int d\mathbf{r} \tilde{\mathbf{e}}(\mathbf{r}) E_2^* E_1^2}{(\int d\mathbf{r} \epsilon_1 |\mathbf{E}_1|^2)(\sqrt{\int d\mathbf{r} \epsilon_2 |\mathbf{E}_2|^2})} \sqrt{\lambda_1^3}, \quad (3)$$

where $\tilde{\mathbf{e}}(\mathbf{r}) = 1$ inside the nonlinear medium and zero elsewhere. Based on the above expressions, one can define the following dimensionless figures of merit:

$$\text{FOM}_1 = Q_1^2 Q_2 |\tilde{\beta}|^2 \left(1 - \frac{Q_1}{Q_1^{\text{rad}}}\right)^2 \left(1 - \frac{Q_2}{Q_2^{\text{rad}}}\right), \quad (4)$$

$$\text{FOM}_2 = (Q_1^{\text{rad}})^2 Q_2^{\text{rad}} |\tilde{\beta}|^2, \quad (5)$$

where FOM_1 represents the efficiency per power, often quoted in the so-called undepleted regime of low-power conversion [30], and FOM_2 represents an intrinsic upper bound that depends only on the *uncoupled* cavity parameters, e.g., the intrinsic radiative lifetimes Q^{rad} . In particular, given a set of radiation loss rates, FOM_1 is maximized when the modes are critically coupled, $Q = \frac{Q^{\text{rad}}}{2}$, in which case $\text{FOM}_1^{\text{max}} = \text{FOM}_2/64$, whereas the absolute maximum occurs in the absence of radiative losses, $Q^{\text{rad}} \rightarrow \infty$, or equivalently, when FOM_2 is maximized. From either FOM, it is clear that, apart from frequency matching and lifetime engineering, the design of optimal SHG cavities rests on achieving a large nonlinear coupling $\tilde{\beta}$.

2. OPTIMIZATION FORMULATION

Optimization techniques have been regularly employed by the photonic device community, primarily for fine-tuning the characteristics of a predetermined geometry; the majority of these techniques involve probabilistic Monte Carlo algorithms, such as particle swarms, simulated annealing, and genetic algorithms [31–33]. While some of these gradient-free methods have been used to uncover a few unexpected results out of a limited number of degrees of freedom (DOFs) [34], gradient-based topology optimization methods efficiently handle a far larger design space, typically considering every pixel or voxel as a DOF in an extensive 2D or 3D computational domain, giving rise to novel topologies

and geometries that might have been difficult to conceive from conventional intuition alone. The early applications of topology optimization were primarily focused on mechanical problems [35] and only recently were expanded to encompass photonic systems, though largely limited to linear devices [34,36–42].

Recent work [37] considered topology optimization of the cavity Purcell factor by exploiting the concept of local density of states (LDOS). In particular, the equivalence between the LDOS and power radiated by a *point* dipole can be exploited to reduce Purcell-factor maximization problems to a series of small scattering calculations. Defining the objective function $\max_{\mathbf{e}} f(\tilde{\mathbf{e}}(\mathbf{r}); \omega) = -\text{Re}[\int d\mathbf{r} \mathbf{J}^* \cdot \mathbf{E}]$, it follows that \mathbf{E} can be found by solving the frequency domain Maxwell's equations $\mathcal{M}\mathbf{E} = i\omega\mathbf{J}$, where \mathcal{M} is the Maxwell operator (Supplement 1) and $\mathbf{J} = \delta(\mathbf{r} - \mathbf{r}_0)\hat{\mathbf{e}}_j$. The maximization is then performed over a discretized domain defined by the *normalized* dielectric function, $\{\tilde{\epsilon}_\alpha = \tilde{\epsilon}(\mathbf{r}_\alpha), \alpha \leftrightarrow (i\Delta x, j\Delta y, k\Delta z)\}$. A key realization in [37] is that, instead of maximizing the LDOS at a single discrete frequency ω , a better-posed problem is that of maximizing the frequency-averaged f in the vicinity of ω , denoted by $\langle f \rangle = \int d\omega' \mathcal{W}(\omega'; \omega, \Gamma) f(\omega')$, where \mathcal{W} is some weight function defined over a specified bandwidth Γ . Using contour integration techniques, the frequency integral can be conveniently replaced by a single evaluation of f at a complex frequency $\omega + i\Gamma$ [37]. For a fixed Γ , the frequency average effectively forces the algorithm to favor minimizing V over maximizing Q ; the latter can be enhanced over the course of the optimization by gradually winding down Γ [37]. A major merit of this formulation is that it features a mathematically well-posed objective as opposed to a direct maximization of the cavity Purcell factor $\frac{Q}{V}$, allowing rapid convergence into extremal solutions.

A simple extension of the optimization problem from single-mode to multimode cavities maximizes the minimum of a collection of LDOS at different frequencies, while the objective becomes: $\max_{\mathbf{e}_a} \min[\text{LDOS}(\omega_1), \text{LDOS}(2\omega_1)]$, which requires solving two *separate* scattering problems, $\mathcal{M}_1 \mathbf{E}_1 = \mathbf{J}_1$ and $\mathcal{M}_2 \mathbf{E}_2 = \mathbf{J}_2$, for the two distinct *point* sources $\mathbf{J}_1, \mathbf{J}_2$ at ω_1 and $\omega_2 = 2\omega_1$, respectively. However, as discussed before, rather than maximizing the Purcell factor at individual resonances, the key to realizing optimal SHG is to maximize the overlap integral $\tilde{\beta}$ between \mathbf{E}_1 and \mathbf{E}_2 , described by Eq. (3). Here, we suggest an elegant way to incorporate $\tilde{\beta}$ by *coupling* the two scattering problems. We consider not a point dipole but an extended source $\mathbf{J}_2 \sim \mathbf{E}_1^2$ at ω_2 and optimize a single combined radiated power $f = -\text{Re}[\int d\mathbf{r} \mathbf{J}_2^* \cdot \mathbf{E}_2]$ instead of two otherwise *unrelated* LDOS calculations. Hence, f yields precisely the $\tilde{\beta}$ parameter along with any resonant enhancement factors ($\sim Q/V$) in \mathbf{E}_1 and \mathbf{E}_2 . Intuitively, \mathbf{J}_2 can be thought of as a nonlinear polarization current induced by \mathbf{E}_1 in the presence of the second-order susceptibility tensor $\chi^{(2)}$, and, in particular, is given by $J_{2i} = \tilde{\mathbf{e}}(\mathbf{r}) \sum_{jk} \chi_{ijk}^{(2)} E_{1j} E_{1k}$ where the indices i, j, k run over the Cartesian coordinates. In general, $\chi_{ijk}^{(2)}$ mixes polarizations, and f is a sum of different contributions from various polarization combinations. In what follows, we focus on the simplest case in which \mathbf{E}_1 and \mathbf{E}_2 have the same polarization, corresponding to a diagonal $\chi^{(2)}$ tensor determined by a scalar $\chi_{\text{eff}}^{(2)}$. Such an arrangement can be obtained by, for example, proper alignment of the crystal orientation axes [18,30]. With this simplification, the generalization of the linear topology-optimization problem to the case of SHG becomes

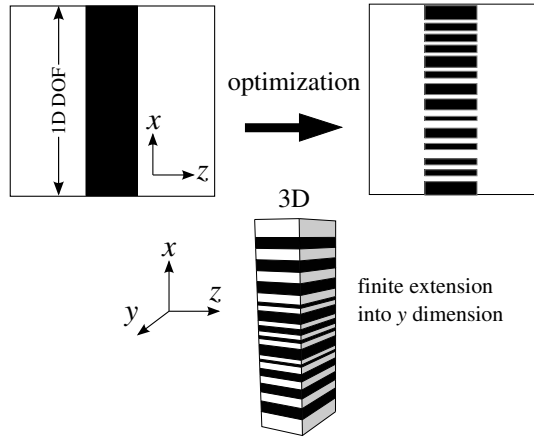


Fig. 1. Work flow of the design process. The DOFs in our problem consist of all of the pixels along the x direction of a 2D computational domain. Starting from a vacuum or uniform-dielectric slab, the optimization seeks to develop an optimal pattern of material layers (with a fixed thickness in the z direction) that can tightly confine light at the desired frequencies while ensuring maximal spatial overlap between the confined modes. The developed 2D cross-sectional pattern is truncated at a finite width in the y direction to produce a fully 3D micropost or grating cavity that is then simulated by FDTD methods to extract the resonant frequencies, quality factors, eigenmodes, and corresponding modal overlaps. Here, it must be emphasized that we merely performed 1D optimization (within a 2D computational problem) because of limited computational resources; consequently, our design space is severely constrained.

$$\begin{aligned} \max_{\bar{\epsilon}_\alpha} \langle f(\bar{\epsilon}_\alpha; \omega_1) \rangle &= -\text{Re} \left[\left\langle \int \mathbf{J}_2^* \cdot \mathbf{E}_2 d\mathbf{r} \right\rangle \right], \\ \mathcal{M}_1 \mathbf{E}_1 &= i\omega_1 \mathbf{J}_1, \\ \mathcal{M}_2 \mathbf{E}_2 &= i\omega_2 \mathbf{J}_2, \omega_2 = 2\omega_1 \end{aligned} \quad (6)$$

where

$$\begin{aligned} \mathbf{J}_1 &= \delta(\mathbf{r}_\alpha - \mathbf{r}_0) \hat{\mathbf{e}}_p, \quad j \in \{x, y, z\} \\ \mathbf{J}_2 &= \bar{\epsilon}(\mathbf{r}_\alpha) E_{1j}^2 \hat{\mathbf{e}}_p, \\ \mathcal{M}_l &= \nabla \times \frac{1}{\mu} \nabla \times -\epsilon_l(\mathbf{r}_\alpha) \omega_l^2, \quad l = 1, 2 \\ \epsilon_l(\mathbf{r}_\alpha) &= \epsilon_m + \bar{\epsilon}_\alpha(\epsilon_{dl} - \epsilon_m), \quad \bar{\epsilon}_\alpha \in [0, 1], \end{aligned}$$

and where ϵ_d denotes the dielectric contrast of the nonlinear medium and ϵ_m is that of the surrounding linear medium. Note that $\bar{\epsilon}_\alpha$ is allowed to vary continuously between 0 and 1; intermediate values are penalized by threshold projection filters [43]. The scattering framework makes it straightforward to calculate the derivatives of f with respect to $\bar{\epsilon}_\alpha$ via the adjoint variable method [35–37]. The optimization problem can then be solved by any gradient-based algorithm, such as the method of moving asymptotes [44].

Figure 1 describes the work flow of our optimization procedure. For computational convenience, the optimization is carried out using a 2D computational cell (in the x – z plane), though the resulting optimized structures are given a finite transverse extension h_y (along the y direction) to make realistic 3D devices (see Fig. 3). In principle, the wider the transverse dimension, the better the cavity quality factors since they are closer to their 2D limit, which consists only of radiation loss in the z direction; however, as h_y increases, $\bar{\beta}$ decreases due to increasing mode volumes. In practice, we chose h_y of the order of a few vacuum wavelengths so as not to greatly compromise either Q or $\bar{\beta}$. We then analyze the 3D structures via rigorous finite-difference time-domain (FDTD) simulations to determine the resonant lifetimes and modal overlaps. By virtue of our optimization scheme, we invariably find that frequency matching is satisfied to within the mode linewidths.

3. OPTIMAL DESIGNS

Table 1 characterizes the FOMs of some of our newly discovered microcavity designs, involving simple micropost and gratings structures of various $\chi^{(2)}$ materials, including GaAs, AlGaAs, and LiNbO₃. The low-index material layers of the microposts consist of alumina (Al₂O₃), while gratings are embedded in either silica or air (see Supplement 1 for details). Note that, in addition to their performance characteristics, these structures significantly differ from those obtained by conventional methods in that traditional designs often involve rings [17,18], periodic structures, or tapered defects [24], which tend to ignore or sacrifice $\bar{\beta}$ in favor of increased lifetimes, and for which it is also difficult to obtain widely separated modes [19]. Figure 2 illustrates one of the optimized structures—a doubly resonant rectangular micropost cavity with alternating AlGaAs/Al₂O₃ layers—along with spatial profiles of the fundamental and harmonic modes. For convenience, we consider modes with the same polarization (major field component E_y): although AlGaAs (similar to GaAs) has a non-vanishing off-diagonal tensor element $\chi_{xyz}^{(2)}$, it can couple the E_y components of fundamental and second-harmonic modes if the crystal plane is appropriately oriented in the (111) direction [19]. The cavity designed by our approach differs from conventional microposts in that it does not consist of periodic bilayers, yet it supports two localized modes at precisely $\lambda_1 = 1.5 \mu\text{m}$ and $\lambda_2 = \lambda_1/2$. In addition to having large $Q^{\text{rad}} \gtrsim 10^5$ and small $V \sim (\lambda_1/n)^3$, the structure exhibits an ultralarge nonlinear coupling $\bar{\beta} \approx 0.018$ that is almost 1 order of magnitude larger than the best overlap found in the literature (see Fig. 3).

An interesting aspect of the optimized structures is the appearance of deeply subwavelength features $\sim 1\%$ – 5% of $\frac{\lambda_1}{n}$, leading to a kind of metamaterial geometry in the optimization direction; we surmise that these arise regardless of starting conditions in order to accommodate a delicate cancellation of the out-going radiation

Table 1. SHG Figures of Merit, Including Frequencies λ , Overall and Radiative Quality Factors Q ; Q^{rad} , and Nonlinear Coupling β Corresponding to the Fundamental and Harmonic Modes of Topology-Optimized Micropost and Grating Cavities of Different Material Systems

| Structure | $b_x \times b_y \times b_z (\lambda_1^3)$ | $\lambda (\mu\text{m})$ | (Q_1, Q_2) | $(Q_1^{\text{rad}}, Q_2^{\text{rad}})$ | $\bar{\beta}$ | FOM ₁ | FOM ₂ |
|-----------------------------------------------------|-------------------------------------------|-------------------------|--------------|----------------------------------------|---------------|-------------------|----------------------|
| (1) AlGaAs/Al ₂ O ₃ micropost | $8.4 \times 3.5 \times 0.84$ | 1.5–0.75 | (5000, 1000) | $(1.4 \times 10^5, 1.3 \times 10^5)$ | 0.018 | 7.5×10^6 | 8.3×10^{11} |
| (2) GaAs gratings in SiO ₂ | $5.4 \times 3.5 \times 0.60$ | 1.8–0.9 | (5000, 1000) | $(5.2 \times 10^4, 7100)$ | 0.020 | 7×10^6 | 7.5×10^9 |
| (3) LN gratings in air | $5.4 \times 3.5 \times 0.80$ | 0.8–0.4 | (5000, 1000) | (6700, 2400) | 0.030 | 8.4×10^5 | 9.7×10^7 |

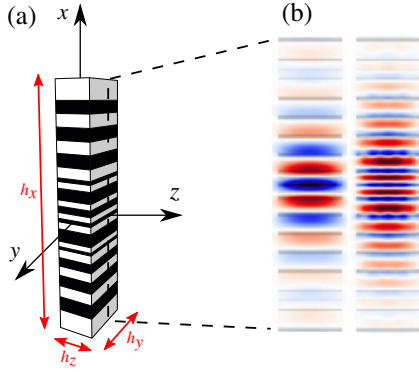


Fig. 2. (a) Schematic illustration of a topology-optimized micropost cavity with alternating AlGaAs/Al₂O₃ layers and dimensions $h_x \times h_y \times h_z = 8.4 \times 3.5 \times 0.84(\lambda_1^3)$. For structural details, please refer to Supplement 1. (b) x - z cross section of the E_y components of two localized modes of frequencies $\lambda_1 = 1.5 \mu\text{m}$ and $\lambda_2 = \lambda_1/2$.

(resulting in high Q) and constructive nonlinear overlap (large β) at the precise designated frequencies. In particular, we find that these features are not easily removable, as their absence greatly perturbs the quality factors and frequency matching. Here, it is worth mentioning that this level of structural sensitivity is typically absent in modes confined by traditional bandgap mechanisms via Bragg scattering [10]. However, to the best of our knowledge, no structure exists that possesses multiple bandgaps with strongly confined modes ($Q > 10^4$) at vastly disparate frequency regimes, not to mention modes that exhibit a large nonlinear overlap. In contrast, topology optimization suggests that one needs very careful interference cancellations enabled by aperiodic arrangement and subwavelength features to simultaneously achieve precise frequency matching and optimal nonlinear overlap.

To understand the mechanism of improvement in $\tilde{\beta}$, it is instructive to consider the spatial profiles of interacting modes. Figure 2(b) plots the y components of the electric fields in the x - z plane against the background structure. Since $\tilde{\beta}$ is a *net* total

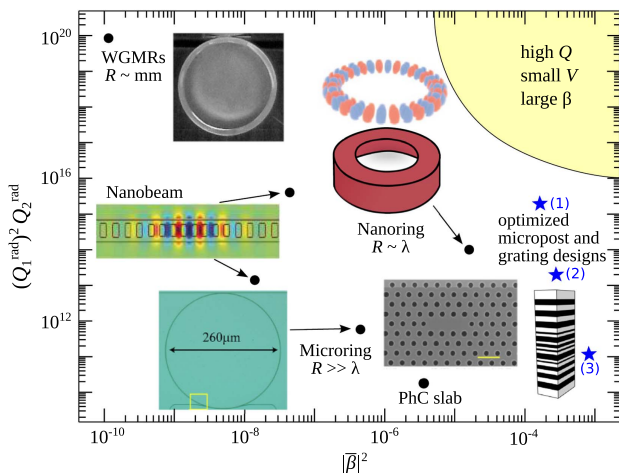


Fig. 3. Scatter plot of $(Q_1^{\text{rad}})^2 Q_2^{\text{rad}}$ versus nonlinear overlap $|\tilde{\beta}|^2$ for representative geometries, including WGMRs [26], microring and nanoring resonators [17,18], photonic crystal slabs, and nanobeam cavities [16,19]. A trend toward decreasing lifetimes and increasing overlaps is observed as devices become increasingly smaller. Meanwhile, it remains an open problem to discover structures with high Q , small V , and large $|\tilde{\beta}|$ (shaded region).

of positive and negative contributions coming from the local overlap factor $E_1^2 E_2$ in the presence of nonlinearity, not all local contributions are useful for SHG conversion. Most notably, one observes that the positions of negative anti-nodes of E_2 (light red regions) coincide with either the nodes of E_1 or alumina layers (where $\chi^{(2)} = 0$), minimizing negative contributions to the integrated overlap. In other words, improvements in $\tilde{\beta}$ do not arise purely due to tight modal confinement, but also from the constructive overlap of the modes enabled by the strategic positioning of field extrema along the structure.

From an experimental point of view, the realization of the multilayer stack is well documented in the literature [45,46]: (i) stacks of Al_xGa_{1-x}As/Al_yGa_{1-y}As layers can be readily grown (metal organic chemical vapor deposition or molecular beam epitaxy), where x and y are chosen so that the layers are lattice matched and also $x \sim 1$ and $y \sim 0$; (ii) the pillar can be defined using electron beam lithography and reactive ion etching (e.g., using Cl-based chemistry); (iii) the structure is placed in the oxidation furnace: then high Al content layers (Al_xGa_{1-x}As) are oxidized and turned into Al₂O₃ (AlO_x, to be precise), whereas low Al content layers are intact. This takes advantage of the well-known fact that large Al content AlGaAs layers can be oxidized much faster than low Al content ones. Additionally, the micropost cavity can be naturally integrated with quantum dots and quantum wells for cavity QED applications [47]. Similar to other wavelength-scale structures, the operational bandwidths of these structures are limited by radiative losses in the lateral direction [10,48,49], but their ultralarge overlap factors more than compensate for the increased bandwidth, which ultimately may prove beneficial in experiments subject to fabrication imperfections and for large-bandwidth applications [1,2,6,50].

Based on the tabulated FOMs (Table 1), the efficiencies and power requirements of realistic devices can be directly calculated. For example, assuming $\chi_{\text{eff}}^{(2)}(\text{AlGaAs}) \sim 100 \text{ pm/V}$ [18], the AlGaAs/Al₂O₃ micropost cavity (Fig. 2) yields an efficiency of $\frac{P_{2,\text{out}}}{P_1^2} = 2.7 \times 10^4 / W$ in the undepleted regime when the modes are critically coupled, $Q = \frac{Q^{\text{rad}}}{2}$. For larger operational bandwidths, e.g., $Q_1 = 5000$ and $Q_2 = 1000$, we find that $\frac{P_{2,\text{out}}}{P_1^2} = 16/W$. When the system is in the depleted regime and critically coupled, we find that a maximum efficiency of 25% can be achieved at $P_1^{\text{crit}} \approx 0.15 \text{ mW}$, whereas, when assuming smaller $Q_1 = 5000$ and $Q_2 = 1000$, a maximum efficiency of 96% can be achieved at $P_1^{\text{crit}} \approx 0.96 \text{ W}$.

4. COMPARISON AGAINST PREVIOUS DESIGNS

Table 2 summarizes various performance characteristics, including the aforementioned FOM, for a handful of previously studied geometries with length scales spanning from millimeters to a few micrometers. Figure 3 demonstrates a trend among these geometries toward increasing $\tilde{\beta}$ and decreasing Q^{rad} as device sizes decrease. Maximizing $\tilde{\beta}$ in millimeter-to-centimeter scale bulky media translates to the well-known problem of phase matching the momenta or propagation constants of the modes [30]. In this category, traditional whispering gallery mode resonators (WGMRs) offer a viable platform for achieving high-efficiency conversion [26]; however, their ultralarge lifetimes (critically dependent upon material-specific polishing techniques), large sizes (millimeter length scales), and extremely weak nonlinear coupling (large mode volumes) render them far from optimal chip-scale devices. Although miniature WGMRs, such as microdisk and

Table 2. SHG Figures of Merit (see Table 1) of Representative, Hand-designed Geometries based on Bang-gap or Index-guided Confinement^a

| Structure | $\lambda(\mu\text{m})$ | (Q_1, Q_2) | $(Q_1^{\text{rad}}, Q_2^{\text{rad}})$ | $\bar{\beta}$ | FOM ₁ | FOM ₂ |
|--------------------------------|------------------------|--------------------------|----------------------------------------|---------------|-------------------------|-------------------|
| LN WGM resonator [26] | 1.064–0.532 | $(3.4 \times 10^7, -)$ | $(6.8 \times 10^7, -)$ | — | $\sim 10^{10}$ | — |
| AlN microring [17] | 1.55–0.775 | $(\sim 10^4, \sim 5000)$ | — | — | 2.6×10^5 | — |
| GaP PhC slab [16] ^b | 1.485–0.742 | $(\approx 6000, -)$ | — | — | $\approx 2 \times 10^5$ | — |
| GaAs PhC nanobeam [19] | 1.7–0.91 ^c | (5000, 1000) | $(> 10^6, 4000)$ | 0.00021 | 820 | 1.8×10^8 |
| | 1.8–0.91 | (5000, 1000) | $(6 \times 10^4, 4000)$ | 0.00012 | 227 | 2.1×10^5 |
| AlGaAs nanoring [18] | 1.55–0.775 | (5000, 1000) | $(10^4, > 10^6)$ | 0.004 | 10^5 | 1.6×10^9 |

^aAlso shown are the FOM₁ and FOM₂ figures of merit described in Eqs. (4) and (5).

^bSHG occurs between a localized defect mode (at the fundamental frequency) and an extended index-guided mode of the photonic crystal (PhC).

^cResonant frequencies are mismatched.

microring resonators [17,27,29], show increased promise due to their smaller mode volumes, improvements in $\bar{\beta}$ are still hardly sufficient for achieving high efficiencies at low powers. Ultracompact nanophotonic resonators, such as the recently proposed nanorings [18], 2D photonic crystal defects [16], and nanobeam cavities [19], possess even smaller mode volumes but prove challenging for design due to the difficulty of finding well-confined modes at both the fundamental and second-harmonic frequencies [16]. Even when two such resonances can be found by fine-tuning a limited set of geometric parameters [18,19], the frequency-matching constraint invariably leads to suboptimal spatial overlaps, which severely limits the maximal achievable $\bar{\beta}$.

Our optimization method seeks to maximize *intrinsic* geometric parameters of an *unloaded* cavity, e.g., Q^{rad} and $\bar{\beta}$, whereas the *loaded* cavity lifetime Q depends on the choice of coupling mechanism, e.g., free-space, fiber, or waveguide coupling, and is therefore an external parameter that can be considered independently of the optimization. When evaluating the performance characteristics, such as FOM₁, we assume total operational lifetimes $Q_1 = 5000$, $Q_2 = 1000$. In comparing Tables 1 and 2, one observes that, for a comparable Q , the topology-optimized structures perform significantly better in both FOM₁ and FOM₂ than any conventional geometry, with the exception of the lithium niobate (LN) gratings, whose low Q^{rad} lead to slightly lower FOM₂. Generally, the optimized microposts and gratings perform better by virtue of a large and robust $\bar{\beta}$ which, notably, is significantly larger than that of existing designs. Here, we have not included in our comparison those structures that achieve non-negligible SHG by special poling techniques and/or quasi-phase-matching methods [29,30,51], though their performance is still suboptimal compared to the topology-optimized designs. Such methods are highly material-dependent and are thus not readily applicable to other material platforms; instead, ours is a purely geometrical topology optimization technique applicable to any material system.

5. CONCLUDING REMARKS

In conclusion, we have presented a formulation that allows for large-scale optimization of SHG. Applied to simple micropost and grating structures, our approach yields new classes of microcavities with stronger performance metrics over existing designs. One potentially challenging aspect for fabrication in the case of gratings is the presence of deeply subwavelength features, which would require difficult high-aspect-ratio etching or growth techniques. Another caveat about wavelength-scale cavities is that they are sensitive to structural perturbations near the cavity center, where most of the field resides. In our optimized structures, the

FOMs are robust to within $\sim \pm 20$ nm variations (approximately one computational pixel). One possible way to constrain the optimization to ensure some minimum spatial feature and robustness is to exploit so-called regularization filters and worst-case optimization techniques [43], which we will consider in future work. However, subwavelength features and structural sensitivity should not be an issue for the micropost cavities since each material layer can be grown/deposited to a nearly arbitrary thickness with angstrom precision [47,48].

Our micropost cavities represent fundamentally new photonic designs obtained by a novel design process—arguably, they could not have been designed from intuition alone. Furthermore, the proposed optimization framework provides a natural versatile tool to tackle various challenging scenarios and exotic applications in nonlinear photonics including, for example, higher-order frequency conversion processes with more than two modes, as well as problems that require conversion of single photons and quantum states of light.

Funding. Air Force Office of Scientific Research (AFOSR) (FA9550-14-1-0389); Army Research Office through the Institute for Soldier Nanotechnologies (W911NF-13-D-0001); National Science Foundation (NSF) (DGE-1144152, DMR-1454836).

See Supplement 1 for supporting content.

REFERENCES

1. K. W. DeLong, R. Trebino, J. Hunter, and W. E. White, "Frequency-resolved optical gating with the use of second-harmonic generation," *J. Opt. Soc. Am. B* **11**, 2206–2215 (1994).
2. M. A. Arbore, A. Galvanauskas, D. Harter, M. H. Chou, and M. M. Fejer, "Engineerable compression of ultrashort pulses by use of second-harmonic generation in chirped-period-poled lithium niobate," *Opt. Lett.* **22**, 1341–1343 (1997).
3. T. F. Heinz, C. K. Chen, D. Ricard, and Y. R. Shen, "Spectroscopy of molecular monolayers by resonant second-harmonic generation," *Phys. Rev. Lett.* **48**, 478–481 (1982).
4. P. S. Kuo, K. L. Vodopyanov, M. M. Fejer, D. M. Simanovskii, X. Yu, J. S. Harris, D. Bliss, and D. Weyburne, "Optical parametric generation of a mid-infrared continuum in orientation-patterned GaAs," *Opt. Lett.* **31**, 71–73 (2006).
5. K. L. Vodopyanov, M. M. Fejer, X. Yu, J. S. Harris, Y.-S. Lee, W. C. Hurlbut, V. G. Kozlov, D. Bliss, and C. Lynch, "Terahertz-wave generation in quasi-phase-matched GaAs," *Appl. Phys. Lett.* **89**, 141119 (2006).
6. R. Krischek, W. Wiczorek, A. Ozawa, N. Kiesel, P. Michelberger, T. Udem, and H. Weinfurter, "Ultraviolet enhancement cavity for ultrafast nonlinear optics and high-rate multiphoton entanglement experiments," *Nat. Photonics* **4**, 170–173 (2010).
7. A. Vaziri, G. Weihs, and A. Zeilinger, "Experimental two-photon, three-dimensional entanglement for quantum communication," *Phys. Rev. Lett.* **89**, 240401 (2002).

8. S. Tanzilli, W. Tittel, M. Halder, O. Alibart, P. Baldi, N. Gisin, and H. Zbinden, "A photonic quantum information interface," *Nature* **437**, 116–120 (2005).
9. S. Zaske, A. Lenhard, C. A. Keßler, J. Kettler, C. Hepp, C. Arend, R. Albrecht, W.-M. Schulz, M. Jetter, P. Michler, and C. Becher, "Visible-to-telecom quantum frequency conversion of light from a single quantum emitter," *Phys. Rev. Lett.* **109**, 147404 (2012).
10. J. D. Joannopoulos, S. G. Johnson, J. N. Winn, and R. D. Meade, *Photonic Crystals: Molding the Flow of Light*, 2nd Ed. (Princeton University, 2008).
11. M. Soljačić, M. Ibanescu, S. G. Johnson, Y. Fink, and J. D. Joannopoulos, "Optimal bistable switching in non-linear photonic crystals," *Phys. Rev. E* **66**, 055601(R) (2002).
12. M. Soljacic, C. Luo, J. D. Joannopoulos, and S. Fan, "Nonlinear photonic crystal microdevices for optical integration," *Opt. Lett.* **28**, 637–639 (2003).
13. M. F. Yanik, S. Fan, and M. Soljacic, "High-contrast all-optical bistable switching in photonic crystal microcavities," *Appl. Phys. Lett.* **83**, 2739–2741 (2003).
14. M. F. Yanik, S. Fan, M. Soljačić, and J. D. Joannopoulos, "All-optical transistor action with bistable switching in a photonic crystal cross-waveguide geometry," *Opt. Lett.* **28**, 2506 (2004).
15. J. Bravo-Abad, A. W. Rodriguez, J. D. Joannopoulos, P. T. Rakich, S. G. Johnson, and M. Soljacic, "Efficient low-power terahertz generation via on-chip triply-resonant nonlinear frequency mixing," *Appl. Phys. Lett.* **96**, 101110 (2010).
16. K. Rivoire, Z. Lin, F. Hatami, W. T. Masselink, and J. Vučković, "Second harmonic generation in gallium phosphide photonic crystal nanocavities with ultralow continuous wave pump power," *Opt. Express* **17**, 22609–22615 (2009).
17. W. H. P. Pernice, C. Xiong, C. Schuck, and H. X. Tang, "Second harmonic generation in phase matched aluminum nitride waveguides and micro-ring resonators," *Appl. Phys. Lett.* **100**, 223501 (2012).
18. Z.-F. Bi, A. W. Rodriguez, H. Hashemi, D. Duchesne, M. Lončar, K.-M. Wang, and S. G. Johnson, "High-efficiency second-harmonic generation in doubly-resonant $X^{(2)}$ microring resonators," *Opt. Express* **20**, 7526–7543 (2012).
19. S. Buckley, M. Radulaski, J. L. Zhang, J. Petykiewicz, K. Biermann, and J. Vučković, "Multimode nanobeam cavities for nonlinear optics: high quality resonances separated by an octave," *Opt. Express* **22**, 26498–26509 (2014).
20. A. Rodriguez, M. Soljačić, J. D. Joannopoulos, and S. G. Johnson, " $X^{(2)}$ and $X^{(3)}$ harmonic generation at a critical power in inhomogeneous doubly resonant cavities," *Opt. Express* **15**, 7303–7318 (2007).
21. V. R. Almeida, C. A. Barrios, R. R. Panepucci, and M. Lipson, "All-optical control of light on a silicon chip," *Nature* **431**, 1081–1084 (2004).
22. Q. Xu and M. Lipson, "Carrier-induced optical bistability in silicon ring resonators," *Opt. Lett.* **31**, 341–343 (2005).
23. J. S. Levy, M. A. Foster, A. L. Gaeta, and M. Lipson, "Harmonic generation in silicon nitride ring resonators," *Opt. Express* **19**, 11415–11421 (2011).
24. P. B. Deotare, M. W. McCutcheon, I. W. Frank, M. Khan, and M. Lončar, "High quality factor photonic crystal nanobeam cavities," *Appl. Phys. Lett.* **94**, 121106 (2009).
25. Z. Lin, S. G. Johnson, A. W. Rodriguez, and M. Lončar, "Design of diamond microcavities for single photon frequency down-conversion," *Opt. Express* **23**, 25279–25294 (2015).
26. J. U. Fürst, D. V. Strekalov, D. Elser, M. Lassen, U. L. Andersen, C. Marquardt, and G. Leuchs, "Naturally phase-matched second-harmonic generation in a whispering-gallery-mode resonator," *Phys. Rev. Lett.* **104**, 153901 (2010).
27. S. Diziain, R. Geiss, M. Zilk, F. Schrepel, E.-B. Kley, A. Tunnermann, and T. Pertsch, "Second harmonic generation in free-standing lithium niobate photonic crystal I3 cavity," *Appl. Phys. Lett.* **103**, 051117 (2013).
28. C. Wang, M. J. Burek, Z. Lin, H. A. Atikian, V. Venkataraman, I.-C. Huang, P. Stark, and M. Lončar, "Integrated high quality factor lithium niobate microdisk resonators," *Opt. Express* **22**, 30924–30933 (2014).
29. P. S. Kuo, J. Bravo-Abad, and S. G. Solomon, "Second-harmonic generation using quasi-phaseshatching in a GaAs whispering-gallery-mode microcavity," *Nat. Commun.* **5**, 3109 (2014).
30. R. W. Boyd, *Nonlinear Optics* (Academic, 1992).
31. W. J. Kim and J. D. O'Brien, "Optimization of a two-dimensional photonic-crystal waveguide branch by simulated annealing and the finite-element method," *J. Opt. Soc. Am. B* **21**, 289–295 (2004).
32. B. S. Darki and N. Granpayeh, "Improving the performance of a photonic crystal ring-resonator-based channel drop filter using particle swarm optimization method," *Opt. Commun.* **283**, 4099–4103 (2010).
33. M. Minkov and V. Savona, "Automated optimization of photonic crystal slab cavities," *Sci. Rep.* **4**, 5124 (2014).
34. A. Gondarenko, S. Preble, J. Robinson, L. Chen, H. Lipson, and M. Lipson, "Spontaneous emergence of periodic patterns in a biologically inspired simulation of photonic structures," *Phys. Rev. Lett.* **96**, 143904 (2006).
35. M. P. Bendose and O. Sigmund, *Topology Optimization* (Springer, 2004).
36. J. Jensen and O. Sigmund, "Topology optimization for nano-photonics," *Laser Photon. Rev.* **5**, 308–321 (2011).
37. X. Liang and S. G. Johnson, "Formulation for scalable optimization of microcavities via the frequency-averaged local density of states," *Opt. Express* **21**, 30812–30841 (2013).
38. D. Liu, L. H. Gabrielli, M. Lipson, and S. G. Johnson, "Transformation inverse design," *Opt. Express* **21**, 14223–14243 (2013).
39. A. Y. Piggott, J. Lu, T. M. Babinec, K. G. Lagoudakis, J. Petykiewicz, and J. Vuckovic, "Inverse design and implementation of a wavelength demultiplexing grating coupler," *Sci. Rep.* **4**, 7210 (2014).
40. H. Men, K. Y. K. Lee, R. M. Freund, J. Peraire, and S. G. Johnson, "Robust topology optimization of three-dimensional photonic-crystal band-gap structures," *Opt. Express* **22**, 22632–22648 (2014).
41. A. Y. Piggott, J. Lu, K. G. Lagoudakis, J. Petykiewicz, T. M. Babinec, and J. Vuckovic, "Inverse design and demonstration of a compact and broadband on-chip wavelength demultiplexer," *Nat. Photonics* **9**, 374–377 (2015).
42. B. Shen, P. Wang, and R. Menon, "An integrated-nanophotonics polarization beamsplitter with $2.4 \times 2.4 \mu\text{m}^2$ footprint," *Nat. Photonics* **9**, 378–382 (2015).
43. F. Wang, B. Lazarov, and O. Sigmund, "On projection methods, convergence and robust formulations in topology optimization," *Struct. Multidiscip. Optim.* **43**, 767–784 (2011).
44. K. Svanberg, "A class of globally convergent optimization methods based on conservative convex separable approximations," *SIAM J. Optim.* **12**, 555–573 (2002).
45. M. H. MacDougall, P. D. Dapkus, A. E. Bond, C.-K. Lin, and J. Geske, "Design and fabrication of VCSELs with Al_xO_y -GaAs DBRs," *IEEE J. Sel. Top. Quantum Electron.* **3**, 905–915 (1997).
46. M. Wu, G. Li, W. Yuen, and C. Chang-Hasnain, "Widely tunable $1.5 \mu\text{m}$ micromechanical optical filter using $\text{AlO}_x/\text{AlGaAs}$ DBR," *Electron. Lett.* **33**, 1702–1704 (1997).
47. M. Lerner, N. Gregersen, F. Dunzer, S. Reitzenstein, S. Hofling, J. Mork, L. Worschech, M. Kamp, and A. Forchel, "Bloch-wave engineering of quantum dot micropillars for cavity quantum electrodynamics experiments," *Phys. Rev. Lett.* **108**, 057402 (2012).
48. K. Vahala, *Optical Microcavities* (World Scientific, 2004).
49. Y. Zhang and M. Lončar, "Sub-micron diameter micropillar cavities with high quality factors and ultra-small mode volumes," *arXiv:0902.2553* (2009).
50. M. Scalora, M. J. Bloemer, A. S. Manka, J. P. Dowling, C. M. Bowden, R. Viswanathan, and J. W. Haus, "Pulsed second-harmonic generation in nonlinear, one-dimensional, periodic structures," *Phys. Rev. A* **56**, 3166–3174 (1997).
51. G. D. Miller, R. G. Batchko, W. M. Tulloch, D. R. Weise, M. M. Fejer, and R. L. Byer, "42%-efficient single-pass cw second-harmonic generation in periodically poled lithium niobate," *Opt. Lett.* **22**, 1834–1836 (1997).